EES Catalysis

PAPER

View Article Online
View Journal | View Issue

Cite this: *EES Catal.*, 2025, 3, 521

On the growth and water oxidation stability of hydrous iridium oxide†

Matej Zlatar, *[ab] Xianxian Xie,[c] Carlo Franke,[d] Tomáš Hrbek,[c] Zdeněk Krtouš,[e] Tong Li,[d] Ivan Khalakhan[c] and Serhiy Cherevko *[a]

Received 6th December 2024,
Accepted 26th February 2025

DOI: 10.1039/d4ey00268g

rsc.li/eescatalysis

Hydrous iridium oxide (HIROF) is a highly active catalyst for the oxygen evolution reaction (OER) with broad application in pH sensing and charge storage devices. However, the mechanisms driving its growth, as well as the associated iridium dissolution, remain incompletely understood. To address this knowledge gap, we employ online inductively coupled plasma mass spectrometry (ICP-MS) to monitor iridium dissolution from sputtered thin films of varying thicknesses during electrochemical cycling. Complementary techniques, including atom probe tomography (APT), ellipsometry, and X-ray photoelectron spectroscopy (XPS), are used to study oxidation states and interface composition. Our findings reveal a tri-phase interface consisting of metallic iridium, compact anhydrous oxide, and hydrous oxide, where dissolution predominantly occurs at the metal–compact oxide interface, driven by transient processes during cycling. HIROF growth strongly depends on iridium grain size, with smaller grains inhibiting growth due to the accumulation of an inner compact IrO_2 layer. This effect is linked to increased oxophilicity, which lowers the reducibility of compact oxide. These insights advance understanding of HIROF growth mechanisms, offering strategies to optimize its performance and stability, particularly in proton exchange membrane water electrolyzers (PEMWEs), where iridium scarcity is critical. Broader implications extend to hydrous oxide formation on other noble and non-noble metals, potentially further advancing other electrochemical applications.

Broader context

Hydrous oxides are used in a variety of electrochemical applications and sustainable energy technologies, including water electrolysis. However, critical gaps in understanding their growth mechanisms and stability hinder their efficient use. Our study focuses on hydrous iridium oxide, a model system notable for its near-complete utilization of iridium compared to crystalline IrO_2, and its relevance to hydrogen crossover in operational proton exchange membrane water electrolyzers (PEMWEs). Addressing these challenges is necessary to reducing iridium usage, a significant barrier to the widespread implementation of PEMWE technology. We propose a novel model for the growth mechanism of hydrous iridium oxide, shedding light on the size-dependent nature of nanoparticle growth and the role of transient interfacial processes in its stability. These insights advance the fundamental understanding of hydrous oxides and provide strategies to improve the performance and sustainability of PEMWEs and other technologies, such as alkaline water electrolysis, where hydrous oxides form on non-noble metals.

1. Introduction

Since its discovery over 60 years ago,[1] electrochemically grown hydrous iridium oxide (HIROF), sometimes referred to as anodic iridium oxide films (AIROF) or electrodeposited iridium oxide films (EIROF),[2] has attracted significant interest. In this work, we use the abbreviation HIROF, consistent with recent publications,[3–5] as it is a broader, more inclusive term independent of the specific growth method. Stonehart *et al.* pioneered early studies by demonstrating that HIROF formation differs from Pt or Au due to its reversible 3D surface oxide formation and reduction.[6] Initially, this was attributed to the reversible chemisorption of oxygen-containing species,[1,7,8]

[a] Forschungszentrum Jülich GmbH, Helmholtz-Institute Erlangen-Nürnberg for Renewable Energy (IET-2), Cauerstrasse 1, 91058 Erlangen, Germany. E-mail: m.zlatar@fz-juelich.de, s.cherevko@fz-juelich.de
[b] Department of Chemical and Biological Engineering, Friedrich-Alexander-Universität Erlangen-Nürnberg, Egerlandstr. 3, 91058 Erlangen, Germany
[c] Department of Surface and Plasma Science, Faculty of Mathematics and Physics, Charles University, V Holešovičkách 2, 180 00 Praha 8, Czech Republic
[d] Faculty of Mechanical Engineering, Atomic-scale Characterisation, Ruhr-Universität Bochum, Universitätsstraße 150, 44801 Bochum, Germany
[e] Department of Macromolecular Physics, Faculty of Mathematics and Physics, Charles University, V Holesovickach 2, 180 00, Prague, Czech Republic

† Electronic supplementary information (ESI) available. See DOI: https://doi.org/10.1039/d4ey00268g

and later to the reversible formation and reduction of an oxide phase.[9] Finally, Gottesfeld *et al.* suggested that this reversible behavior is not associated with metal oxidation or reduction but with a redox process within the film.[10] Following this fundamental works, numerous studies have focused on understanding HIROF's charge storage mechanisms,[11,12] structure,[13,14] conductivity[10,15] and pH-sensitivity.[16,17]

HIROF is generally described as a gel-like material comprising chains of oxygen-bridged hydroxy-aqua complexes of iridium (hydrated oxy-hydroxide species).[18–20] Its structure is often compared to the open polymeric network of α- and γ- forms of hydrous nickel oxyhydroxides.[21] Still, the precise composition and structure of HIROF remain subjects of ongoing debate.[22–24] Unlike HIROF, the crystalline rutile phase of IrO_2 features a rigid, extended crystalline network with stronger Ir–O bonds, fewer bulk defects and vacancies, and a lower surface concentration of active sites.[5] Structurally, rutile IrO_2 adopts a tetragonal unit cell with edge-sharing octahedral linkages, where each Ir ion is octahedrally coordinated by six oxygen atoms,[25] resulting in a denser, more compact structure with greater stability compared to the corner-sharing octahedral linkages in HIROF.[23]

In order to optimize the structure and properties of HIROF, extensive research has focused on understanding its electrochemical growth mechanism. Unlike with Pt[26] or Au,[27] HIROF formation on Ir requires potential cycling (scans[13,21,28–31] or pulses[18,32–35]) rather than a constant applied potential.[6,31] This is likely attributable to the lower potentials in case of iridium (<2.0 V_{RHE}), given that the oxygen evolution reaction (OER) starts even before 1.6 V_{RHE}.[36] Nevertheless, a recent study has demonstrated that hydrous oxide formation can still be achieved using a series of constant potentials.[37] While potential pulsing typically results in faster growth rates than cyclic scans,[18] both methods demonstrate a strong dependence on the upper and lower potential limits.[18,30,32,35] This dependency was attributed to the substantial reduction and re-oxidation of the compact oxide necessary for the growth.[21] For consistency with prior literature on this topic[16,18,19] this work refers to this type of oxide as the compact oxide, even though it is sometimes called anhydrous oxide.[38] However, its precise structure requires further investigation through advanced spectroscopic techniques.

One of the earliest proposed mechanisms for HIROF growth was the pit model, introduced by Otten and Visscher.[39] They suggested that oxidation of metallic Ir occurs at specific active sites, penetrating locally into the underlying metal and forming so-called "pits".[39] However, the pit model failed to explain the constant or even decreasing H_{upd} observed during cycling. Rand and Wood proposed that the decrease in H_{upd} and the increase in oxide peak currents are linked. They suggested that the formation of an irreversible oxide phase, not completely reducing at 0 V_{RHE}, leads to a decrease in H_{upd}. Hence, the charge passed in the oxygen region was associated with reversible changes in oxide stoichiometry. This mechanism assumes electron exchange between the oxide layer and the underlying metal.[28] However, authors incorrectly concluded that the hydrous oxide layer possesses good metallic conductivity.[40,41]

Following studies have challenged these models, proposing alternative mechanisms such as dissolution/precipitation[13] and incomplete reduction due to strong Ir–O bonds.[30,31] Dissolution/precipitation was ruled out by demonstrating that growth rates were independent of diffusion layer thickness.[13,30] In contrast, incomplete reduction failed to explain the hydration of unreduced oxide. Another proposed model, similar to that of Pt or Au, suggested a structure with a compact anhydrous inner layer and dispersed hydrous outer layer.[16] This model proposed that oxygen species discharge and water penetrate the compact oxide layer during the anodic scan. In the cathodic scan, the compact oxide is reduced, displacing metal atoms that re-oxidize during the following anodic scan, driving the growth process. However, it remained unclear why these re-oxidized metal atoms form hydrous oxide rather than a compact one.

While previous models have faced challenges, the model proposed by Pickup and Birss offered a compelling explanation for HIROF growth. According to this model, the compact oxide layer partially hydrates at positive and reduces at negative potentials, while the hydrous oxide layer remains.[18] Despite all of this, HIROF stability has received the least attention. Cherevko *et al.* recently addressed this knowledge gap,[42] proposing that iridium dissolution during HIROF growth predominantly occurs at the metal–compact oxide interface due to transient processes.[43]

A complete understanding of the HIROF growth mechanism is important due to its broader implications. Hydrous oxides, similar to those observed in iridium,[44] forms on other noble metals[6,45] (Pt,[46,47] Rh,[48] Au,[49] Ru[50]) and non-noble metals (Co, Ni, Fe, Mo).[14,38,51,52] Therefore, HIROF growth mechanism might serve as a model system for studying the transition from monolayer to multilayer oxide phases.[13] Insights gained from studying HIROF can be applied in optimizing its stability and improving performance in applications including electrochromic displays,[53,54] neural stimulating electrodes,[55,56] electrochemical capacitors,[57] and pH sensors.[17,58,59] Moreover, HIROF could potentially be used at the anode side of the proton exchange membrane water electrolyzers (PEMWEs) due to iridium's high catalytic activity for the OER.[60] Although ruthenium and its oxide are more active, iridium's superior stability under acidic conditions at high anodic potentials makes it the preferred choice for commercial application.[61] As the world transitions towards renewable energy sources to address the climate change, PEMWEs are becoming increasingly important for energy storage.

Currently, widespread implementation of PEMWEs is hindered by the high cost of iridium, primarily due to its scarcity.[62] To address this challenge, reducing the amount of iridium required is essential. One promising solution is in the superior OER activity of HIROF compared to traditional catalysts.[29] This improved activity has been attributed to the presence of Ir^{III} species and vacancies within the HIROF lattice,[63] as well as the higher concentration of electrophilic oxygen species on its surface.[64] While the exact mechanisms underlying HIROF's high activity are still discussed, it is clear that hydrous iridium oxide offers almost complete utilization. In contrast, only 1–2% of atoms are active in crystalline IrO_2.[65] Although HIROF seems promising, its stability during oxygen evolution at high current densities remains a concern,[42,66,67] posing challenges for its long-term application in practical devices.

Previously, HIROF was studied on bulk polycrystalline Ir electrodes,[13,14,18,30,33,42] which may not accurately represent the nanoparticles used for practical application in electrolyzers. Therefore, in this study, we prepared sputtered metallic Ir thin films with varying thicknesses as our model system. This approach allowed us to restrict the amount of metallic Ir and investigate the interfaces between metallic Ir, compact oxide, and hydrous oxide during HIROF growth. More specifically, we examined whether metallic Ir remains at the core or is fully oxidized into HIROF, while also investigating the associated dissolution processes. In contrast to the predominantly electrochemical methods and lack of post-mortem characterizations found in the literature, we employed scanning flow cell coupled to inductively coupled plasma mass spectrometry (SFC-ICP-MS). This was complemented by advanced physical surface-sensitive techniques such as X-ray photoelectron spectroscopy (XPS), atomic force microscopy (AFM), ellipsometry, and atom probe tomography (APT).

2. Experimental section

2.1. Magnetron sputtering

Samples were prepared using a magnetron sputtering system with three circular TORUS magnetrons (Kurt J. Lesker) positioned at a 45° angle to the substrate. Initially, a 10 nm thick titanium layer was deposited using a 2″ Ti target (99.99%, Kurt J. Lesker). Following this, a 100 nm thick gold layer was deposited using a 2″ Au target (99.99%, Safina) without sample exposure to the air. Subsequently, iridium layers of various thicknesses (1, 3, 5, 10, and 20 nm) were deposited using a 2″ Ir target (99.99%, Kurt J. Lesker), with the thickness controlled by adjusting the deposition time.

2.2. Physical characterization

2.2.1. Atomic force microscopy (AFM). Morphology was examined using a MultiMode 8 Atomic Force Microscope (AFM) from Bruker in tapping mode under ambient conditions. SCANASYST-AIR probes (Bruker) with a nominal tip radius of 2 nm were used. Image processing was carried out using NanoScope 1.9 software.

2.2.2. Scanning electron microscopy (SEM). The morphology was examined using a Mira 3 microscope from Tescan operating at the primary electron energy of 30 keV.

2.2.3. Energy-dispersive X-ray spectroscopy (EDX). The composition and elemental mapping were determined by EDX using an XFlash detector from Bruker integrated directly into the SEM.

2.2.4. X-Ray photoelectron spectroscopy (XPS). X-Ray photoelectron spectroscopy (XPS) measurements were conducted using an EnviroESCA device from SPECS. The X-rays were produced by a monochromated Al K_α source with an energy of 1486.71 eV. A Phoibos 160 NAP 1D-DLD hemispherical electron analyzer (SPECS) was employed to measure the energy of the emitted photoelectrons. The pass energy was set to 20 eV, with a measurement step of 0.1 eV and a dwell time of 0.3 seconds per point. The device's construction allows one to pick an exact spot (300 μm diameter) for the analysis. The measured core-level spectra were processed using the KolXPD software.

2.2.5. Atom-probe tomography (APT). The sputtered metallic Ir thin films were initially pretreated in a 50 mL solution of 0.1 M $DClO_4$ in a three-electrode bulk cell. The electrolyte was prepared by diluting concentrated perchloric acid-d solution (68 wt% in D_2O, 99 atom% D, Merck) in 50 mL of D_2O (min 99.9% deuteration degree, Merck). A graphite rod was used as the counter, while an Ag/AgCl electrode was used as the reference electrode. The metallic Ir films, used as working electrodes, were connected using copper tape and immersed in the electrolyte solution. All electrodes were connected to a Biologic VSP-300 potentiostat (Biologic) for electrochemical measurements. After completing the experiments, the electrodes were vacuum-sealed (ALLPAX 265) to minimize exposure to air. Following the electrochemical pretreatment, APT specimens were prepared by using a lift-out procedure in an FEI Helios G4 CX focused ion beam/scanning electron microscope (FIB/SEM). Before ion milling, the thin film samples were capped by a 180 nm Cr protective layer *via* physical vapor deposition in a Leica EM ACE600 sputter coater to protect the sample surfaces, and then a 20 μm (length) × 2 μm (width) × 1 μm (depth) Pt film on top of the Cr protective layer *via* electron beam deposition in FIB/SEM. Afterward, the region of interest was lifted out, and the horizontal lifted-out bar was rotated vertically to ensure the Ir/Au interfaces were at the center of needle-like specimens by rotating the nanomanipulator 180 degrees. Afterward, the samples were transferred to a Si microtip coupon and shaped into needles with a diameter of less than 100 nm by annular milling. APT experiments were performed in laser mode using a Cameca LEAP 5000 XR. A temperature of 60 K, a laser pulse energy of 30 pJ, and a pulse rate of 125 kHz with a detection rate of 0.3% were used as experimental settings. The reconstruction of APT data was performed using the commercial software AP Suite 6.3.0.90.

2.2.6. Ellipsometry. The measurements were done using a Woollam M-2000DI spectroscopic ellipsometer at three angles ranging from 50° to 70° and in the wavelength range of 192–1690 nm. The ellipsometry data were fitted using CompleteEASE software (J. A. Woollam). The reference samples were fitted using the Drude model. The Drude model is typically used to fit the optical properties of metals, particularly mirror-like thin films, such as silver and gold. It is generally applicable in the infrared (IR) region for most known materials, although additional intra- and interband transitions can occur in the visible region.

$$\varepsilon(\omega) = \varepsilon_\infty - \frac{{\omega_p}^2}{\omega^2 + i\gamma\omega}$$

The sample under investigation has a metallic appearance similar to silver or aluminum, suggesting the absence of significant interband transitions in the visible range. Therefore, the ellipsometry data were initially fitted using only the Drude model and an ε_∞ (high-frequency dielectric constant) parameter. This simplified approach captures the core behavior of the dielectric function without introducing unnecessary complexity.

These reference data served as the first layer in the complete model, in which optical parameters were not fitted. A second layer was required for comprehensive fitting. The second layer was modeled using the Tauc–Lorentz approach, which is effective for materials exhibiting a mix of transparent and absorbing properties near the band edge of disordered or amorphous materials.

$$\varepsilon_2(E) = \frac{A \times (E - E_g)^2}{E^2 \times (B^2 - E^2)^2 + C \times E^2}$$

2.3. Stability measurements (SFC-ICP-MS)

Electrochemical measurements and simultaneous metal ion dissolution analyses were conducted using a custom-designed Scanning Flow Cell (SFC) coupled with an Inductively Coupled Plasma Mass Spectrometer (ICP-MS, PerkinElmer NexION 350X). The electrolyte solution, 0.05 M H_2SO_4, was prepared by diluting concentrated H_2SO_4 (96%, Merck Suprapure) in ultrapure water (18.2 MΩ cm, TOC < 3 ppb) and purged with argon throughout each experiment. The electrolyte was then pumped through the SFC and into the ICP-MS at a flow rate of approximately 3.5 μL s^{-1}, regulated by the peristaltic pump of the ICP-MS. A glassy carbon rod (HTW, Sigradur G) was used as the counter electrode, and a double-junction Ag/AgCl electrode (Metrohm) was used as the reference electrode, with the same electrolyte solution in the outer junction. The working electrode, sputtered metallic Ir thin film models, were positioned using an XYZ translation stage (Physik Instrumente) to ensure precise alignment with the 0.01 cm^2 SFC opening. All three electrodes were connected to a Gamry Reference 600 potentiostat (Gamry Instruments), and the measured potentials were calibrated to the reversible hydrogen electrode (RHE) scale. For the dissolution analysis, the ICP-MS was optimized and calibrated daily with standard solutions containing the target elements at concentrations of 0.5, 1, and 5 ppb (Certipur ICP-MS Standard, Merck). Internal standards, such as ^{187}Re, with ionization potentials and atomic masses similar to those of the analytes, were introduced to correct for potential instrument drift and polyatomic interferences. Dissolution data were normalized to the electrolyte flow rate to account for day-to-day variations, while all current densities were normalized to the geometric surface area of the electrodes (mA cm^{-2}). The applied electrochemical protocol is outlined in the following Fig. 1.

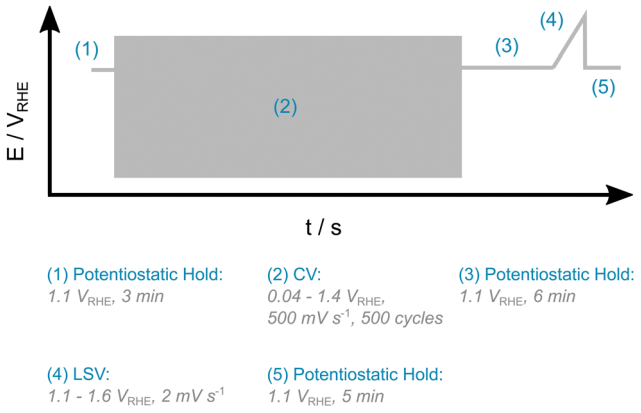

Fig. 1 Electrochemical protocol for SFC-ICP-MS measurements to investigate HIROF growth.

3. Results

To understand how particle size affects HIROF formation, we prepared thin iridium films with varying nominal thicknesses corresponding to different grain sizes (Fig. S1, ESI†). We use the term ''grain sizes'' rather than ''particle sizes'' because, unlike solution-based nanoparticles, magnetron-sputtered thin films consist of surface-bound grains rather than discrete particles. In thinner films, these grains are initially separated by voids, but as film thickness increases, they become more compact and elongated. Therefore, ''grain size'' is the more appropriate term to describe the structural units within the films.

Real-time iridium dissolution during HIROF growth was monitored using an SFC-ICP-MS setup. Previously, it was shown that iridium dissolves during the formation of hydrous oxides on bulk Ir films,[42] hypothesized to originate from the interface between metal and freshly formed compact oxide, based on a model of Birss and Pickup.[18] In this work, we investigate this interface using thin films, where the amount of metallic Ir depends on the film thickness. This approach allows us to test the proposed model and better understand Ir dissolution during HIROF growth.

The electrochemical protocol (Fig. 1) started with a 3-minute hold at 1.1 V_{RHE} to minimize initial dissolution due to metal oxidation or reduction of native oxides on the films.[68] This was followed by 500 cyclic voltammetry (CV) cycles ranging from 0.04 to 1.4 V_{RHE} at a scan rate of 500 mV s^{-1}, following established procedures for HIROF formation.[18,20,28]

3.1. Formation and dissolution dynamics of HIROF studied by SFC-ICP-MS

Fig. 2(a) shows a typical CV of metallic iridium.[31,69,70] The initial electrochemical active surface area (ECSA), estimated from the third cycle's H_{upd} region, correlates well with film thickness (Fig. S2, ESI†). Thinner films exhibit lower ECSA, while thicker films (10 and 20 nm) show higher values, indicating increased roughness and surface area. The extent of iridium oxidation/reduction (around 0.95 V_{RHE}), which is proportional to the amount of iridium on the electrode surface, also increases with film thickness (Fig. 2(a)). Further details are provided below.

After completing 500 cycles, characteristic peaks emerged on the CVs (Fig. 2(b)), including a smaller peak appearing around 0.65 V_{RHE}. The origin of this peak has been previously discussed[71] and is reported to decrease with higher HIROF thickness.[19] For a more detailed explanation regarding this and related hypotheses from the literature, refer to the discussion section of this manuscript. The most pronounced peak, around 0.97 V_{RHE}, corresponds to the $Ir^{III} \leftrightarrow Ir^{IV}$ redox transition,[18,19,31,42] confirming HIROF formation on the metallic iridium surfaces. This was

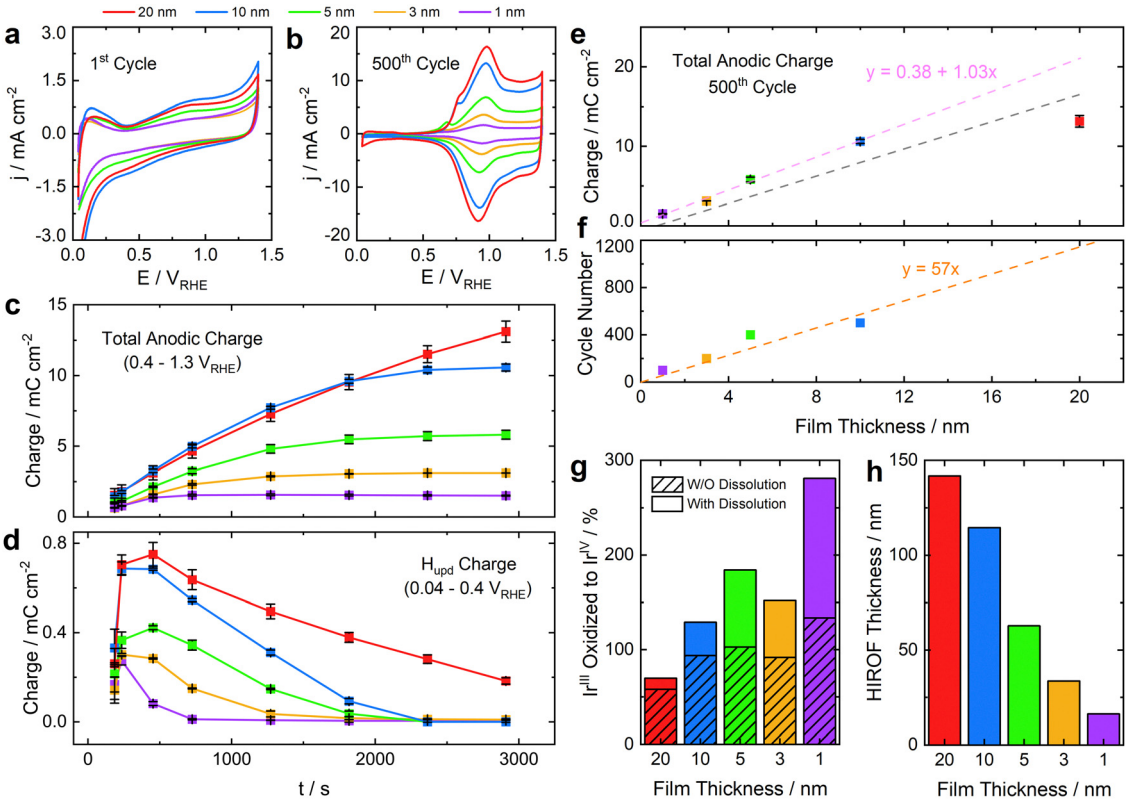

Fig. 2 Electrochemical analysis of HIROF formation as a function of Ir grain size. (a) Initial cycle, (b) 500th cycle (cyclic voltammetry from 0.04–1.4 V_{RHE} at 500 mV s^{-1}). (c) Total anodic charge (0.4–1.3 V_{RHE}) and (d) H_{upd} charge (0.04–0.4 V_{RHE}) across selected cycles. (e) Total anodic charge at the 500th cycle depending on nominal film thickness. The pink dashed line represents a linear fit of the measured points, while the gray dashed line represents a linear fit of the theoretical charge, assuming 100% oxidation of metallic Ir and accounting for dissolution (see below). (f) Cycle number at which HIROF growth ceases for each film thickness, determined by fitting data points from Fig. 2(c) with a sigmoidal function and analyzing its second derivative. (g) Percentage of Ir oxidized from the III to IV, assuming 100% oxidation of metallic Ir, with and without accounting for dissolution. (h) HIROF thickness, calculated based on the total anodic charge at the 500th cycle relative to the prepared film thickness.

further supported by SEM-EDX analysis (Fig. S3, ESI†), showing that the larger grains, originating from the underlying Au layer, were no longer visible after cycling, with the appearance of oxygen on the surface. Furthermore, the charge under the CVs at the 500th cycle increases with the nominal thickness of the thin films (Fig. 2(b)).

To explore this further, we integrated the total anodic charge in the range from 0.4 to 1.3 V_{RHE} (Fig. 2(c)), which is associated with a rough estimation of the amount of formed oxide,[42] and the amount of active sites potentially involved in OER.[72,73] The 1.3 V_{RHE} value was chosen because of potential overlap with the $Ir^{IV} \leftrightarrow Ir^{V}$ redox transition at higher values. However, the exact potential and extent of this transition at 1.3 V_{RHE} remains uncertain.[74] Additionally, this integration range represents a practical compromise as double-layer capacitance and pseudocapacitance overlap in this region, making clear separation difficult.

As previously reported, the integrated total anodic charge reached a plateau for all samples except for the 20 nm film, where deviation from the linear trend is observed.[19,42] Notably, the thinner the metallic Ir films, the earlier this plateau was reached during the cycling. Plotting the total anodic charge at the 500th cycle against the nominal film thickness revealed that thicker metallic Ir films, corresponding to larger grain sizes, exhibited higher total anodic charges or thicker HIROF layers (Fig. 2(e)). A similar trend was observed in Fig. 2(c), likely reflecting an increased number of active sites or a greater availability of metallic iridium for HIROF formation. The relationship appears linear for all samples except the 20 nm thick sample, which deviates from the expected trend. Additionally, for this sample, HIROF saturation is not reached even after 500 cycles. By performing a linear fit and extrapolating the total anodic charge values for 1–10 nm thick samples (pink dashed line), we estimate that if the 20 nm film reached saturation (Fig. 2(e)), the total anodic charge would be 20 mC cm^{-2} instead of the observed 13 mC cm^{-2}. This suggests that nearly 65% of the metallic Ir film is converted to HIROF. Based on a slope of linear fit, each increase in grain size after 500 cycles results in an additional 1.03 mC cm^{-2} of total anodic charge (or HIROF thickness). The *y*-intercept value of the linear fit, 0.38 mC cm^{-2}, likely corresponds to the double-layer charge of compact iridium oxide, representing the case where the metallic Ir thickness is zero.

By fitting a sigmoidal function to the data points in Fig. 2(c) and analyzing its second derivative, we can determine the cycle number at which growth ceases for each grain size (Fig. 2(f)). Based on a linear extrapolation of the data for thinner films,

approximately 1140 cycles would be required for the 20 nm thin film to reach HIROF saturation and the corresponding total anodic charge predicted in Fig. 2(e). This indicates that the growth rate of HIROF on thicker metallic Ir films slows significantly after 500 cycles. Based on the linear fit in Fig. 2(e) (dashed pink line), and assuming a constant growth rate, 1140 cycles would result in approximately 150% conversion of metallic Ir to HIROF.

To calculate the theoretical loading, we used the SFC-measured surface area (0.01 cm^2) and the nominal thickness of the films to estimate the spot volume. From the density of metallic Ir (ρ = 22.56 g cm^{-3}),[75] we derived theoretical loadings (see calculation 1 in the ESI†). Then, using Faraday's law, we calculated the expected charge if all Ir underwent the $Ir^{III} \leftrightarrow Ir^{IV}$ transition (see calculation 2 in the ESI†). By dividing the total anodic charge at the 500th cycle from Fig. 1(e) and 2(c) by this value, we estimated that in the case of 20 nm thick metallic Ir films, approximately 58%, while in the case of 1 nm film, 134% of the film is oxidized to HIROF (stripped bars, Fig. 2(g)).

The number of Ir surface atoms converted to HIROF per cycle was estimated by dividing the difference in total anodic charge between cycles by the charge per Ir surface atom (calculated according to ref. 18) and is shown in Fig. S4 (see calculation 3 in the ESI†). While the number of Ir atoms converted to HIROF varies during the initial cycles, it stabilizes at approximately 0.05 by the 10th cycle. This value is lower than the 0.4 reported in previous work, where pulses resulted in faster HIROF growth.[18] From cycle 10 to 500, the conversion of Ir surface atoms to HIROF remains relatively constant for the 20 nm film, but decreases with increasing cycle number for the thinner films.

Using Faraday's law, the total anodic charge from the CV, and the molar mass of HIROF,[34,74] we also estimated the mass of HIROF formed. Using a previously determined HIROF density of 2 g cm^{-3} (based on combined optical and coulometric measurements),[74] we calculated the HIROF thickness to be approximately 140 nm for the 20 nm Ir film and 16 nm for the 1 nm film (Fig. 2(h)). This explains why the underlying Au grain morphology is not visible in the HIROF-covered samples shown in Fig. S3 (see calculation 4 in the ESI†).

Additionally, ellipsometry measurements (Fig. S5, ESI†) were also used to determine HIROF thickness.[29,39,76] Details of the applied models are provided in Section 2.2.4. Despite the limitations in fully characterizing the optical properties of these materials, we have confidence in the calculated thickness values. Various modeling approaches were tested, and consistent trends across different models validated the reliability of the measurements. Fig. S5a and b (ESI†) present an example of the measured data for a 20 nm thick sample, while Fig. S5c and d (ESI†) show the refractive index and extinction coefficients for the Drude and Tauc–Lorentz models. The Drude model effectively captures the metallic nature of the thin films, while the Tauc–Lorentz model accounts for the optical changes due to surface modifications, highlighting a combination of transparent and absorbing behavior near the band edge. HIROF thicknesses before and after electrochemical cycling are presented in Fig. S5e (ESI†). The measured thickness of the metallic Ir films aligns well with the target values, while the measured HIROF thickness differs from the electrochemically calculated values, as also observed using SEM.[13] This discrepancy was attributed to microporosity within the HIROF, restricted electrochemical accessibility, and surface-limited redox processes, which collectively yield a larger voltammetrically inferred thickness than that observed by more direct methods such as SEM or ellipsometry. However, the trend aligns reasonably well with the calculated values, showing an increase in HIROF thickness with the increasing thickness of the metallic Ir film. Importantly, metallic Ir remained beneath the HIROF layer.

Fig. 2(d) shows the integrated H_{upd} charge (corresponding to the number of metallic iridium sites available for hydrogen adsorption, similar to platinum) plotted against the number of cycles. However, because iridium does not achieve complete hydrogen coverage, the charge value must be adjusted by a factor of 0.65 to accurately calculate the roughness factor (R_f), real surface area, and ECSA.[18,31,70] Initial dissolution increased roughness and, consequently, ECSA.[71] However, the H_{upd} charge subsequently decreased with cycling, and to a greater extent than reported in other studies.[18,28,34,77] This trend mirrors the previously observed increase in total anodic charge (Fig. 2(c)). Notably, the H_{upd} charge decreased to zero for all samples except the 20 nm film, paralleling the plateau in total anodic charge.

To further illustrate this, the H_{upd} charge is plotted against the total anodic charge in Fig. S6 (ESI†). Although the H_{upd} charge initially increases with the total anodic charge and the cycle number for all samples, it gradually decreases to zero with continued cycling. This decline is more pronounced for smaller grains, whereas no such decline is observed for the 20 nm grains.

Given the established link between HIROF formation and iridium dissolution,[42] and considering the observed variation in cycle number at which HIROF growth appears to cease for different metallic Ir film thicknesses, we investigated this relationship using online ICP-MS (Fig. 3).

The dissolution profiles (Fig. 3(a)) show earlier declines for thinner films, with dissolution decreasing nearly linearly with decreasing film thickness (Fig. 3(b)). Normalizing the dissolution data to theoretical loadings (Fig. 3(c)) reveals that, on average, approximately half of the nominal iridium loading is lost during cycling, especially for the thinner films.

Initially, we estimated that approximately 58% of the 20 nm thick metallic Ir film and 134% of the 1 nm film were oxidized to HIROF (stripped bars, Fig. 2(g)) by dividing the total anodic charge at the 500th cycle with the calculated charge, assuming all Ir underwent the $Ir^{III} \leftrightarrow Ir^{IV}$ transition (see calculation 2 in the ESI†). However, we recalculated the expected charge using Faraday's law after including dissolution data from ICP-MS (Fig. 3(b)) and adjusting the theoretical loading. This correction showed that approximately 70% of the 20 nm was oxidized to HIROF (solid bars, Fig. 2(g)), contrary to the lower values initially determined. This estimate aligns well with the linear fitting from Fig. 2(e), where nearly 65% conversion to HIROF was predicted. Considering that 17% of metallic Ir is dissolved

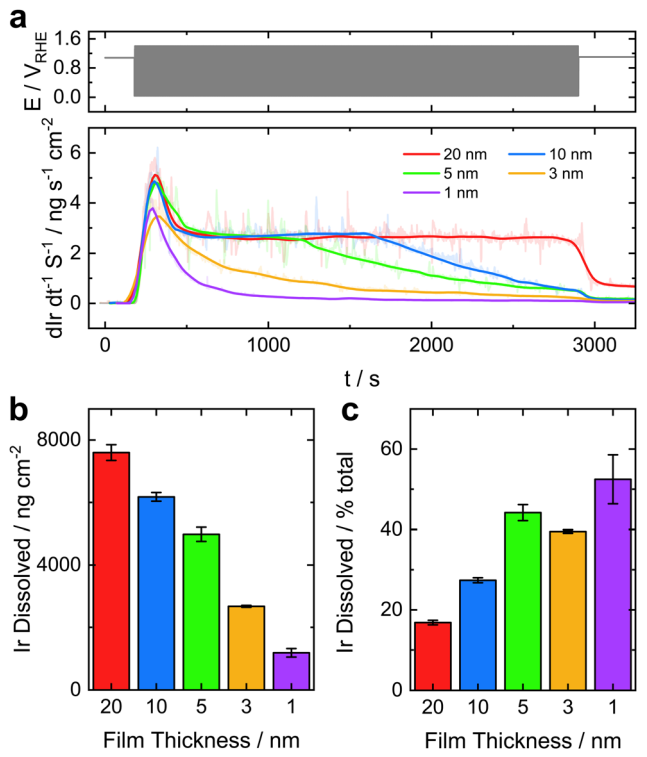

Fig. 3 Impact of Ir grain size on Ir dissolution during HIROF formation: (a) applied potential (top) and resultant dissolution profiles measured by SFC-ICP-MS (bottom). (b) Total dissolution over 500 cycles. (c) Normalized Ir dissolution by theoretical total loading.

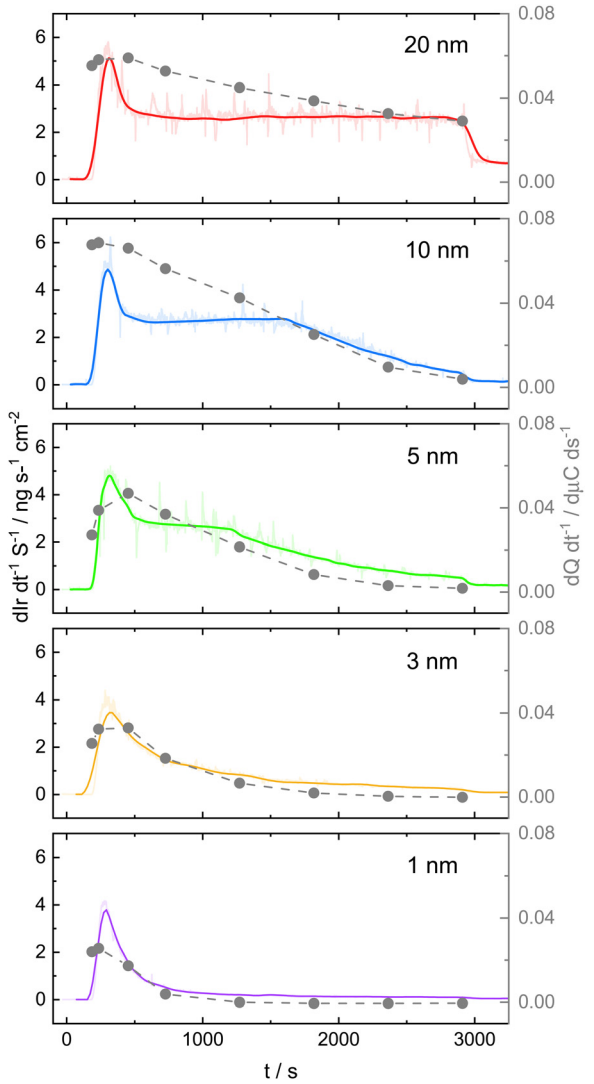

Fig. 4 Correlation between Ir dissolution and HIROF growth. Left *y*-axis: Dissolution rate; right *y*-axis: first derivative of total anodic charge from Fig. 2(c).

(Fig. 3(c)), the remaining 13% likely consists of metallic Ir and/or compact oxide. This is also supported by the observed H_{upd} charge (Fig. 2(d)), which suggests that metallic Ir is still present. In contrast, similar estimations for other thin films (ranging from 10 nm to 1 nm) indicate that the conversion to HIROF exceeds 100% (Fig. 2(g)), suggesting no metallic Ir remains. This observation is consistent with the zero H_{upd} charge values observed in Fig. 2(d). By plotting the charge estimated for the $Ir^{III} \leftrightarrow Ir^{IV}$ transition, accounting for dissolution, and applying a linear fit, we obtain the gray dotted line in Fig. 2(e). It becomes evident that the oxidation rate decreases as the thickness of the metallic Ir film increases (and the thickness of the formed hydrous layer).

Additionally, we calculated the first derivative of the total anodic charge, representing HIROF growth, and overlaid it with the dissolution rate from ICP-MS (Fig. 4).

HIROF growth, as indicated by the rate of increase in the total anodic charge, stops at the same time as decline in Ir dissolution, suggesting a correlation between the two. Given that the dissolution rates in Fig. 3(a) are similar for the 20, 10, and 5 nm samples, we assumed that the compact oxide reduction/oxidation rate is comparable across these films. This implies that the amount of hydrous oxide formed per cycle is consistent for all samples, aligning with the data shown in Fig. S4 (ESI†). Extrapolating this to the 3 nm sample, we can estimate the inflection point of dissolution, as observed for the 10 and 5 nm samples.

Assuming spherical nanoparticle sizes of 10, 5, and 3 nm, we estimate they consist of approximately 37 000, 4600, and 1000 iridium atoms (see calculation 5 in the ESI†). Using the atomic density of 111 plane in an FCC crystal structure and the surface area of the nanoparticle, the number of surface atoms is calculated as 4903, 1226, and 441 for the 10, 5, and 3 nm sizes. Additionally, since hydrous oxide forms from the compact oxide on the surface of metallic iridium, we account for the difference in densities (22.56 g cm^{-3} for metallic Ir and 11.66 g cm^{-3} for IrO_2), estimating that approximately 50% fewer iridium atoms would remain on the surface after oxidation. The 5% surface atom conversion rate per cycle (Fig. S4, ESI†) suggests that complete conversion of all metallic iridium in the nanoparticles would occur after approximately 303, 153, and 91 cycles for the 10, 5, and 3 nm grains, respectively. If we instead assume hemispherical grains (more likely to be exposed to the electrolyte), complete conversion will occur earlier, at around 201, 100, and 62 cycles (see calculation 5.1 in the ESI†).

However, these calculations do not align with the experimental data, which shows that both dissolution and HIROF growth cease later. Specifically, dissolution stopped at the 295th, 225th, and 82nd cycles (Fig. 3(a)) for the 10, 5, and 3 nm films, respectively, with HIROF growth decreasing at the same cycle for a limited time (Fig. S4, ESI†), before halting at the 500th, 400th, and 200th cycle (Fig. 4). Nor do they match the ellipsometry results (Fig. S5, ESI†), which still detect the presence of metallic Ir. This discrepancy indicates that other mechanisms may be contributing to the observed behavior.

3.2. Analysis of HIROF by XPS and APT

To investigate this discrepancy further, we utilized surface characterization techniques such as XPS to investigate the correlation between dissolution during HIROF formation and electrochemical data.

Following electrochemical treatment, XPS measurements (Fig. S7a, ESI† left) reveal a shift in Ir 4f peaks across all samples from the typical binding energy (BE) of metallic iridium at 60.8 eV to a higher oxidation state at 62.2 eV. This BE is higher than the typical value for IrO_2 (61.8 eV) but lower than Ir^{III} in $IrCl_3$ (62.5 eV). Hydrated Ir^{III} oxide is reported to have a BE 0.4–0.5 eV higher than IrO_2 (around 62.4 eV) due to hydration, which agrees well with our XPS results and the electrochemical data.[14,78,79] Additionally, no significant differences were observed when calculating the ratios of Ir^{3+}/Ir^{4+} species on the surfaces. These findings suggest that no metallic Ir remains, indicating complete oxidation to HIROF. However, if a monolayer of metallic Ir were present beneath several nanometers of HIROF, XPS would likely be insufficiently sensitive to detect it. Therefore, while XPS results imply full oxidation, they do not entirely rule out the presence of a thin metallic Ir layer beneath the HIROF.

By deconvolution of the O 1s spectra of the prepared samples, three distinct peaks at 530, 531.5, and 532.9 eV could be fitted (Fig. S7a middle, ESI†), attributed to oxide, hydroxide, and water, respectively.[79] Native oxides formed on the surface during air exposure likely contributed to the presence of oxide and hydroxide.[68] After electrochemical treatment, only peaks for adsorbed water and hydroxide remained (Fig. S7a right, ESI†), indicating the removal of native oxide through reduction or dissolution during HIROF formation.[42]

Additionally, we integrated the O 1s and Ir 4f peaks and calculated the O/Ir ratios. After excluding the adsorbed water peak, the initial O/Ir ratio was approximately 0.3 (Fig. S7b, ESI†), attributed to the presence of native oxide. Following electrochemical treatment, the ratio increased to 3 for the 20 nm sample, consistent with expectations for a HIROF layer (Fig. S7c, ESI†).[78] The trend of exponentially increasing O/Ir ratios with decreasing nominal film thickness (Fig. S7c, ESI†) aligns with previous observations.[14] O/Ir ratios exceeding 4, particularly in thinner films, can be attributed to two factors. One possibility is the presence of OH and H_2O groups within the film, though this is less probable. A more plausible explanation is surface contamination from –OH, SO_4^{2-} (from the electrolyte), and carbon–oxygen species (OH–C, C–O, O═C–O), which become more significant in thinner HIROF films due to increased surface sensitivity.[14,78] Therefore, we refrain from drawing strong conclusions from this data.

To further probe the interface between metallic iridium and the HIROF layer and their oxidation states, we attempted XPS depth profiling. We etched surface layers using an Ar^+ ion beam to expose subsurface oxidation states. However, this method consistently revealed the metallic iridium phase at similar depths across all samples. We concluded that the Ar^+ ion beam reduced the HIROF through chemical interaction or iridium ion redeposition, rendering this method unsuitable for our analysis.

To circumvent the limitations encountered with XPS depth profiling, we employed atom probe tomography (APT) to analyze the surface hydrous oxide and subsurface anhydrous oxide layer. APT is a mass spectrometer technique that provides three-dimensional elemental distribution with a sub-nanometer spatial resolution (detailed experimental procedures are shown in the experimental section and Fig. S8 and S9, ESI†). To resolve the surface hydroxyl groups and water molecules in the HIROF, we conducted electrochemical measurements using deuterated perchloric acid ($DClO_4$) diluted with deuterium oxide (D_2O) to a concentration of 0.1 M.[80] This helped differentiate between electrochemically formed layers and potential contaminants (such as water in humid air) introduced during sample transport or hydrogen from the ultra-high vacuum chamber.

For APT analysis, we examined 20 nm and 2 nm Ir films deposited on Au-coated Si wafer substrates. The 20 nm Ir samples showed low experimental yield in APT due to the increased likelihood of mechanical failure in the specimens, likely caused by the thicker HIROF layer. Despite using vertical FIB lift-out to improve the success rate of APT specimen preparation,[80] these challenges persisted. As a result, we focused on the newly prepared 2 nm thick sample to investigate whether metallic Ir remained beneath the HIROF layer and to understand why its growth ceased, in contrast to the 20 nm sample.

The results are presented in Fig. 5(a) and (b), which offer detailed visualizations of the interface structure. In Fig. 5(a), a 2D analysis shows that the topmost layer comprises a mixture of OD and D_2O integrated with hydrated iridium oxide (IrO_x) above the metallic iridium layer. Fig. 5(b) presents 1D concentration profiles, clearly showing that the formed HIROF layer has a thickness of approximately 6 nm, followed by a 1 nm compact anhydrous oxide layer. This is indicated by the concentrations of D_2O and OD, which drop to zero beyond the 6 nm mark. Underneath these layers, the metallic Ir becomes evident as the O concentration significantly decreases and the Ir signal increases. The vertical APT specimen preparation allows 2 nm deposited Ir to be measured, where the HIROF/compact oxide/Ir/Au interfaces are aligned parallel to the APT analysis direction. Thus, the interface possibly suffers from a subtle trajectory aberration in the later plane across the interfaces. This results in a slight increase in the thickness of each layer. Nevertheless, the observed HIROF thickness of approximately 6 nm is within a similar range to the theoretical 15 nm calculated for a 1 nm thick film (Fig. 2(h)) and the 3 nm measured by ellipsometry (Fig. S5, ESI†).

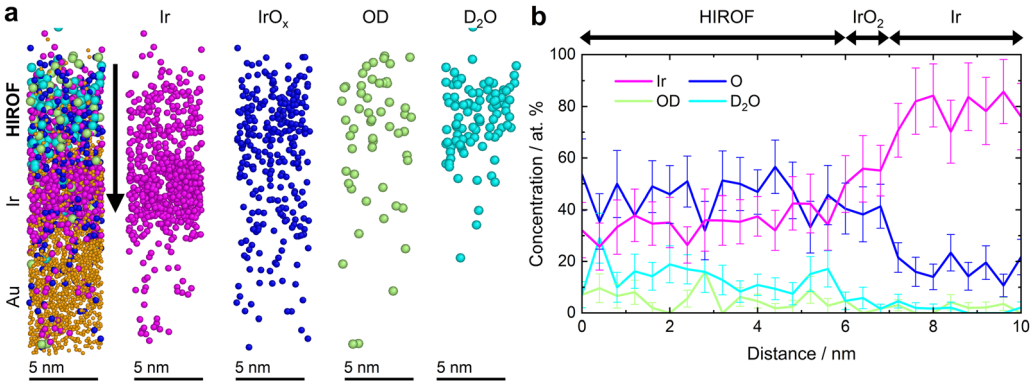

Fig. 5 Atomic interface analysis post-HIROF formation on 2 nm thick film. (a) 2D interface analysis. (b) 1D concentration profiles (OD, D_2O, Au, and Ir) after 500 cycles.

3.3. OER activity and stability of HIROF

Despite the well-documented high activity of amorphous Ir oxides, their lower stability compared to rutile IrO_2 poses challenges for electrolyzer applications.[66,67] To study the impact of HIROF growth on metallic Ir, we compared its performance to pure metallic Ir films without HIROF (Fig. 6 and Fig. S10, S11, ESI†).

As expected, HIROF films demonstrate significantly higher OER activity (Fig. 6(c)) than metallic Ir (Fig. S11c, ESI†), with activity increasing proportionally to thickness (Fig. 2(h)). In contrast, the OER activity of metallic Ir films remains largely unaffected by thickness, with minor variations likely attributed to differences in surface area (Fig. S2, ESI†). Furthermore, compared to commercially used rutile IrO_2, both the thinnest and thickest HIROF films exhibit an overpotential at 1 mA cm^{-2} that is 120–170 mV lower than IrO_2 thin films.[66] By normalizing the activity against the total anodic charge at the 500th cycle (Fig. 2(c)), the LSV profiles are observed to align (Fig. S10a, ESI†). However, deviations at higher overpotentials can be attributed to gas bubble formation. Additionally, a previous study suggested that limitations in mass transfer (from water to active sites and protons from the oxide matrix) and changes in local pH due to trapped protons could also contribute.[42] The observed overlap of activities confirms that ECSA scales almost linearly with activity at lower overpotentials, as shown before for oxygen,[33,42] and chlorine evolution reactions.[13] This is also in line with a recent study showing that the OER activity of amorphous IrO_x exhibits negligible structure sensitivity.[81]

To understand the relationship between iridium dissolution and OER activity, we correlated electrochemical data with dissolution profiles measured using online ICP-MS (Fig. 6(a) and Fig. S11a, ESI†). We found that while dissolution of metallic Ir varies between samples (Fig. S11b, ESI†), influenced by surface area variations (Fig. S2, ESI†) and aligning with activity trends (Fig. S11c, ESI†), the presence of HIROF resulted in increased dissolution and a relatively constant rate regardless of its thickness (Fig. 6(b)). Furthermore, the baseline dissolution signal during LSV for the 20 nm thick sample is significantly higher than that of the other samples. Unlike thinner films, dissolution in this sample persisted throughout all 500 cycles without stabilizing (Fig. 3(a)). Therefore, the holding time at 1.1 V_{RHE} before LSV measurements was insufficient to allow dissolution to return to baseline levels observed in the other samples (Fig. S12, ESI†).

S-numbers, which represent the ratio of evolved O_2 to dissolved Ir, provided additional insights into the stability of HIROF.[66] As HIROF growth (Fig. 2(b) and (c)) and iridium dissolution continued throughout the 500 cycles in the 20 nm sample (Fig. 3(a)), we expected a different S-number than other samples, where both processes were more constrained. However, contrary to expectations, no significant deviation is observed in Fig. 6(d). Instead, HIROF S-numbers increase almost linearly with

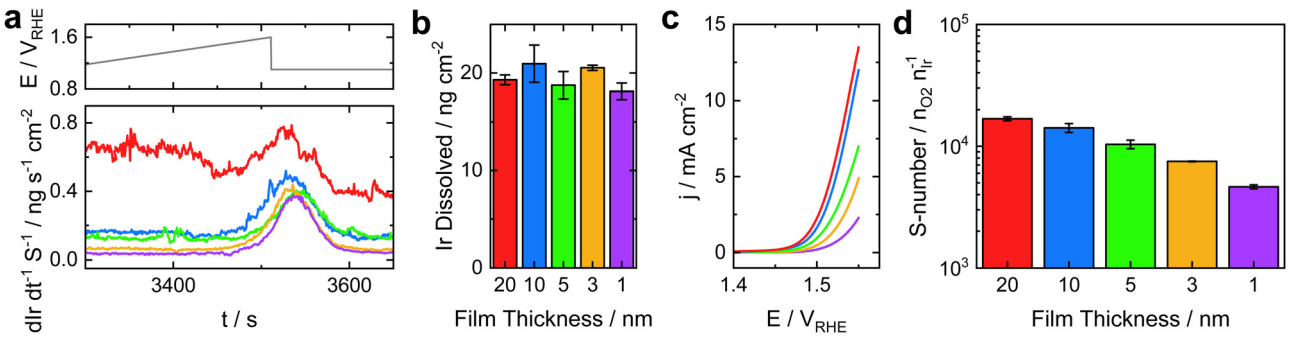

Fig. 6 Activity and stability of HIROF during OER: (a) applied potentials (top) and corresponding dissolution profiles (bottom) measured by SFC-ICP-MS. (b) Total iridium dissolution during LSV, estimated by integrating dissolution profiles from (a). (c) Surface area-normalized LSV, performed in the potential range of 1.2–1.6 V_{RHE} at 2 mV s^{-1}. (d) Stability numbers of Ir, calculated using dissolution data from (b) and charge integrated from (c).

the nominal thickness of metallic Ir films, mirroring the linear increase in current density. In contrast, S-numbers for metallic Ir films without HIROF remain largely unchanged across different thicknesses (Fig. S11d, ESI†). When comparing the values, the S-numbers of the thinnest HIROF films are within the range observed for metallic Ir films, while the thickest HIROF films exhibit values that are nearly an order of magnitude higher. Nevertheless, these values remain approximately two orders of magnitude lower than those reported for IrO_2 thin films.[66]

We hypothesized that transient processes, such as the oxidation of Ir^{3+} to Ir^{4+} or Ir^{4+} to higher oxidation states, occurring at the interfaces between the metal, compact oxide, and hydrous oxide layers, influence dissolution. These interfaces vary between samples, impacting the extent of these transient processes and lowering the S-numbers. This also suggests that the interfaces remain present beneath the formed HIROF. If dissolution was solely related to OER, we would expect a decrease alongside current density, resulting in constant S-numbers (assuming a shared intermediate).[36] Therefore, S-numbers remain the same for metallic Ir films without HIROF, where interfaces and transient processes are similar.

Observations from Fig. 6(a) and Fig. S11a (ESI†) further validate this hypothesis, showing consistent dissolution onset potentials for both metallic Ir films and HIROF across all samples. However, while the dissolution onset for metallic Ir films closely aligns with the OER onset, this is not observed for most HIROF samples (Fig. S10b, ESI†). Specifically, only the 20 nm HIROF sample follows this pattern. In the case of other samples, the OER onset shifts to higher potentials, indicative of thinner HIROF layers, while the dissolution onset remains unchanged, suggesting a more pronounced contribution of transient processes.

4. Discussion and outlook

This section begins by revisiting the well-established Pickup and Birss model of HIROF growth,[18] which we refine in light of our new experimental observations. We then explore how the thickness of the metallic Ir film influences HIROF formation, the loss of H_{upd} features, and the impact of the Gibbs–Thomson effect. Building on these observations, we link our findings to iridium dissolution and the formation of a less permeable inner oxide layer, discussing their combined impact on OER stability. Finally, we consider how these insights might apply to other hydrous oxides on noble and non-noble metals, and we propose future research directions to deepen our understanding of HIROF growth and stability.

We start our discussion by exploring the Pickup and Birss model of HIROF growth (Fig. 7).[18] According to this model, hydrous oxide formation initiates with the development of a compact inner oxide layer, designated as IrO_2, *via* a place-exchange mechanism. At higher potentials, the outer monolayer oxidizes and hydrates (IrO_2OH). During the cathodic scan, the compact oxide reduces back to metal, while the hydrated oxide remains, held by weak electrostatic and van der Waals forces. This cycle results in the formation of a tri-layer interface in the following scan: the inner oxide, a hydrated surface layer, and the bulk hydrous oxide from the previous cycle. The process repeats, with the inner oxide reducing and the hydrated layer merging into the bulk hydrous oxide, driving HIROF growth.

Building on this model, we provide further insights based on our experimental data. Thinner metallic Ir films showed earlier hindrance of HIROF growth (Fig. 2(b) and (c)). The observed decrease in H_{upd} charge (Fig. 2(d)) and Ir dissolution rate (Fig. 3(a)) supports the hypothesis of partial or complete oxidation/dissolution of the metallic core. This hypothesis aligns with a recent study on size-dependent HIROF growth on iridium nanoparticles, which showed that nanoparticles smaller than 5 nm are fully converted to HIROF during cycling.[82] However, since our study demonstrates that Ir dissolves during HIROF growth, and considering the highly porous media used in the mentioned study (as opposed to the flat surface in our work), we propose that dissolved species from larger nanoparticles may not be efficiently removed during the process. This could lead to the precipitation of smaller particles without a metallic core. To validate this mechanism with certainty, an identical-location TEM study tracing individual nanoparticles throughout the cycling process would be necessary.[83]

Therefore, the hypothesis of complete dissolution of the metallic core is ruled out, as only 50% of the total iridium loading dissolved in the 1 nm film (Fig. 3(c)). Additionally, both ellipsometry (Fig. S5, ESI†) and APT (Fig. 5) confirm the presence of metallic Ir beneath the HIROF layer, indicating that full oxidation of the metallic core is unlikely. This conclusion is further supported by calculations based on spherical nanoparticles and the conversion of Ir atoms to HIROF, which reveal that both dissolution and HIROF growth cease later then predicted for complete conversion of the metallic core. This suggests neither complete dissolution nor full oxidation occurs, leading us to explore alternative mechanisms.

Although metallic Ir is present beneath the HIROF layer, the complete disappearance of H_{upd} for most samples remains puzzling (Fig. 2(d)). Previous studies mostly focused on explaining the presence of H_{upd} beneath thick HIROF layers. Buckley and Burke's hypothesis of complete outer layer reduction during the cathodic scan[32] contradicts the accepted HIROF growth mechanism.[18] A more plausible explanation involves the accessibility of metal sites beneath a porous oxide layer,[20,34,45,48] aligning with Pickup and Birss model[18] and supported by the observed porosity of HIROF.[74]

To explain the absence of H_{upd} in our study, we propose that the accumulation of a less permeable inner oxide layer,[74] due to its incomplete reduction in each cycle, may block metallic Ir sites from adsorbing hydrogen.[71] This could explain the observed H_{upd} disappearance (Fig. 2(d)), as the extent of compact oxide reduction during HIROF formation remains unclear. While some studies suggest complete reduction at low potentials[18] others report incomplete reduction that depends on the potential.[42]

The smaller Ir nanoparticles in our thinner films (Fig. S1, ESI†) likely contribute to the accumulation of a less permeable inner oxide layer. This is probably due to the increased surface

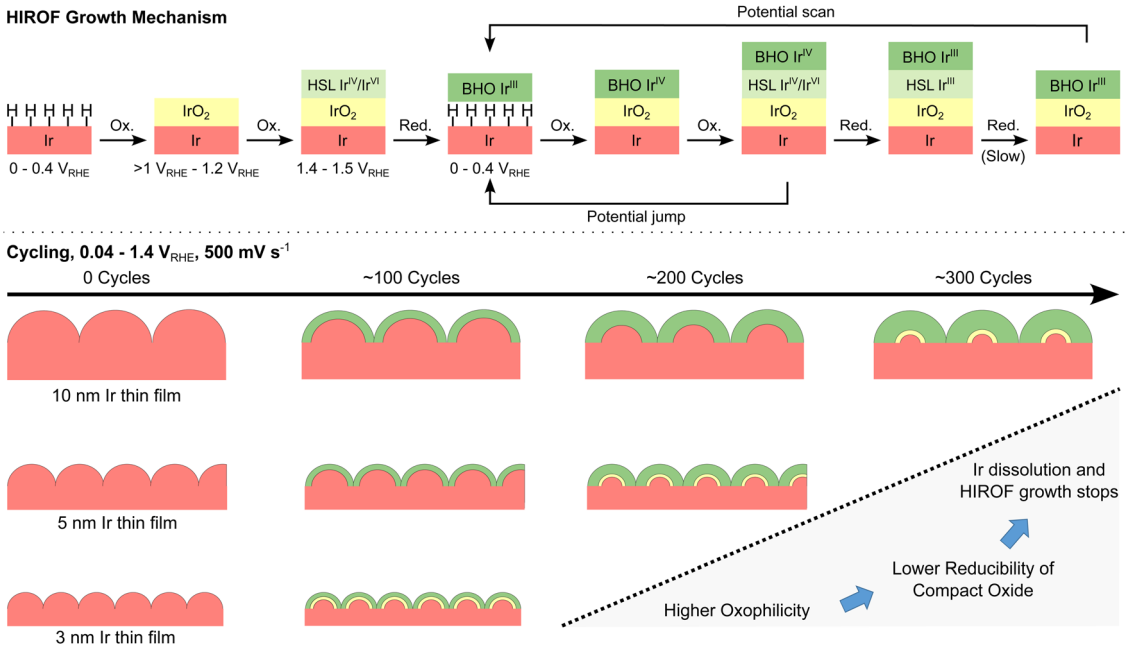

Fig. 7 Summary of previously proposed HIROF growth mechanisms and new insights from this study (HSL: hydrated surface layer, BHO: bulk hydrous oxide).

energy and chemical potential of smaller nanoparticles (higher curvature), as predicted by the Gibbs–Thomson effect. This often results in notable differences in properties such as melting temperature, solubility (resulting in Ostwald Ripening), and electrochemical stability.[84,85] The higher surface energy of smaller nanoparticles also increases their oxophilicity, leading to lower reducibility of the inner compact oxide layer at the same applied potential.[86] Consequently, the compact oxide layer accumulates on the surface and impedes HIROF growth (Fig. S4, ESI†), as newly formed inner layers are more readily hydrated than aged ones, according to Pickup and Birss.[18]

A less reducible compact oxide layer also hinders iridium dissolution (Fig. 3(a)), with the rate remaining constant as long as the reduction/oxidation of the compact oxide remains unchanged (before the inflection point). This aligns with Cherevko *et al.*'s hypothesis that dissolution during HIROF growth is transient and predominantly occurs at the metal–compact oxide interface due to the reduction of the compact oxide.[42] The same mechanism also accounts for the decrease in H_{upd} noted in other studies,[18,28,34,77] typically accompanied by constant[33,45,87] or slightly increased double-layer capacitance.[18] Notably, in our experiments, the decrease in H_{upd} is more pronounced (50–100%, Fig. 2(d)) compared to the 20–30% typically reported for bulk electrodes, further demonstrating the impact of the Gibbs–Thomson effect.

This pronounced impact of the Gibbs–Thomson effect on the properties of thinner films is further supported by the observed lower S-numbers (Fig. 6(d)). As discussed in Section 3.3, lower S-numbers are attributed to the increased contribution of transient processes. The hindered HIROF growth (Fig. S4, ESI†) and the lower S-numbers suggest a more pronounced interface beneath the HIROF in thinner films. This pronounced interface, likely amplified by the Gibbs–Thomson effect due to the increased curvature of the smaller nanoparticles, provides additional sites for these transient processes to occur. A schematic summary of this proposed mechanism is presented in the bottom panel of Fig. 7.

Determining the exact thickness of the compact oxide layer presents a significant challenge. Previous calculations suggest that 1.5 monolayers of metallic Ir oxidize into Ir^{IV}, forming three layers of IrO_2 at 1.2 V_{RHE}.[18] Furthermore, about half of the surface Ir atoms are estimated to convert to hydrous oxide at 1.4 V_{RHE}. This conversion primarily occurs from the inner oxide layer, implying that nearly all Ir atoms in a single layer of IrO_2, or particularly its outer monolayer, are converted.[18] Similar calculations indicate that approximately 5% of surface Ir atoms are converted to HIROF per cycle in our study. This lower value compared to previous publications is likely due to our use of cyclic scans instead of pulses.

Nevertheless, HIROF thickness was estimated in our study (Fig. 2(h)), showing that approximately 140 nm of HIROF formed atop the 20 nm metallic Ir film. We also estimated its thickness using ellipsometry, showing ~45 nm of HIROF forms on the surface. Theoretical calculations suggest that only about 70% of the metallic Ir film was oxidized (Fig. 2(g)) and 17% dissolved (Fig. 3(c)), leaving an estimated 13% of metallic Ir still intact beneath the HIROF, or 30% as estimated by ellipsometry (Fig. S5e, ESI†). Based on our assumption in Fig. 2(f), approximately 1140 additional cycles would be required to oxidize the remaining metallic Ir completely.

In contrast, for the 1 nm metallic Ir films, approximately 15 nm of HIROF was formed (Fig. 2(h)), or ~2.5 nm according to ellipsometry. Again, based on our calculations, around 280% of the metallic Ir was converted to HIROF (Fig. 2(g)). This seems implausible as roughly 50% of the metallic Ir was also dissolved during the process (Fig. 3(c)). Additionally, APT confirms that metallic Ir persists beneath the 2 nm thin HIROF layer (Fig. 5).

Contrary to data shown in Fig. 4, the first derivative of the total anodic charge over time should remain constant if we assume a steady oxidation rate of HIROF. However, a clear decrease is observed, indicating that some form of inhibition is occurring. Additionally, the fraction of metallic Ir that appears to be oxidized varies with film thickness, with thinner films exhibiting higher oxidation rates (Fig. 2(e) and (g)). All samples except the 20 nm film show oxidation percentages exceeding 100%. This apparent ''over-oxidation'' suggests that multi-electron processes may be at play, meaning the number of electrons (n) assumed in Faraday's law calculations (see calculation 2 in the ESI†), particularly for thinner films, should potentially exceed one.

Such multi-electron processes could arise from previously unaccounted oxidation states (*e.g.*, Ir^{I} or Ir^{II}) or involve reversible pathways that extend beyond single-electron transfers. Additionally, higher oxidation states may form before the onset of OER. Although the formal potential for the Ir^{IV} to Ir^{V} transition is quite high, excited Ir^{IV} sites may form Ir^{V} intermediates below the typical redox potential.[88] This explanation aligns with the observed decrease in S-numbers for thinner HIROF films (Fig. 6(d)), where such transient processes are likely more dominant and decrease stability.

The presence of a pre-peak in CVs for thinner films (Fig. 2(b)) might provide some explanation, but it still remains unexplained. Initial hypotheses attributed this feature to transitions between Ir^{III} and Ir^{IV} involving sulfate anions.[19,30] Recent studies, however, suggest alternative mechanisms such as the formation of IrOOH,[89] water electroadsorption at the interface between the inner and hydrous oxide layer,[71] or oxidation of Ir^{III} sites near the metal-oxide boundary.[90] We propose that this pre-peak could also be linked to the oxidation of Ir^{0} to Ir^{x+} (where x could be 1 or 2). This would also support our hypothesis that the oxidation of metallic Ir to HIROF involves a multi-electron transfer (more than one electron), which could explain why the observed oxidation exceeds 100% of the metallic Ir. Additionally, this process is also likely associated with transient dissolution that contributes to the lower S-numbers. Notably, this pre-peak is absent in the 20 nm thin film samples, further supporting its correlation with specific electrochemical transitions in thinner films.

Given the recent challenges in developing new catalysts that outperform existing commercial options in the last decade, it becomes rather important to focus on improving the stability and understanding of promising materials such as HIROF. With the ultimate goal of reducing Ir loadings in real devices, which is currently limited by decreased stability and conductivity, HIROF could provide better utilization and more active sites using the same loadings. Additionally, HIROF could be employed as a precatalyst for OER.

Future research should explore the size-dependent growth of HIROF on nanoparticles in greater detail, using advanced techniques such as synchrotron X-ray diffraction (XRD) and evaluating these materials in real devices. For instance, hydrous oxide layers can be grown on metallic iridium or precipitated as $Ir(OH)_3$ from $IrCl_3$ and KOH, enabling an assessment of how particle size influences both catalytic activity and long-term stability. Stabilizing the tri-layer interface formed during HIROF growth is particularly important, as larger particle sizes appear to mitigate transient dissolution at this interface and thus improve durability. Further improvements could be achieved through strategies such as alloying to modulate oxophilicity or optimizing catalyst–support interactions to improve stability and performance. This focus on stabilizing the oxide layers is especially critical given that hydrous oxide formation and dissolution can be triggered by reduction–reoxidation cycles during hydrogen crossover.

Beyond iridium, the insights gained from this work may extend to other noble metals (*e.g.*, Pt,[46,47] Rh,[48] Au,[49] Ru[50]) and non-noble metals (*e.g.*, Co, Ni, Fe, Mo),[14,38,51,52] where similar hydrous oxides have been reported.[6,45] Consequently, the HIROF growth mechanism described here could serve as a model for understanding the transition from monolayer to multilayer oxide phases in a broader range of metal systems. However, it is important to note that dissolution behaviors, particularly in non-noble metal systems like Ni, may differ significantly and warrant further investigation to determine the relevance of these findings for specific applications.

5. Conclusion

In this work, we investigated the mechanism behind the formation and growth of HIROF layers on metallic iridium. We tested the previously proposed model of HIROF growth on metallic Ir[18] by limiting its amount and employing advanced characterization techniques such as SFC-ICP-MS, ellipsometry, and APT. So far, complete oxidation/dissolution of the metallic core, accumulation of inner compact oxide, and even a decrease in hydration at inner HIROF layers were thought to be responsible for stopping hydrous growth.[71,91] Our most important conclusions can be summarized as follows:

- The dissolution rate of iridium during HIROF growth is constant and is directly related to the rate of compact oxide reduction and oxidation.
- The extent of HIROF oxidation is thickness-dependent, with lower oxidation observed in thicker HIROF layers.
- The inflection point in iridium dissolution, accompanied by a decrease in HIROF growth, is attributed to increased oxophilicity and decreased reducibility of the compact oxide layer, driven by the Gibbs–Thomson effect in smaller nanoparticles.
- The limited growth of HIROF on smaller nanoparticles may make them more promising for OER applications.

Data availability

The authors declare that the data supporting the findings of this study are available within the paper and its ESI.† The processed electrochemical, ICP-MS, and XPS datasets presented in the main manuscript are available at GitHub database (**https://github.com/zlatarmt/Research-Data**). Additionally, raw SEM, AFM, EDX and XPS data are also available at

https://doi.org/10.5281/zenodo.14333437. Any further data can be provided from authors upon request.

Conflicts of interest

There's no conflict of interest to declare.

Acknowledgements

C. Franke and T. Li thank Zentrum für Grenzflächendominierte Höchstleistungswerkstoffe (ZGH) at Ruhr University Bochum for the access of infrastructure (Cameca LEAP 5000 XR and FEI Helios G4 CX SEM/FIB). XX, TH and IK acknowledge support by the project ''The Energy Conversion and Storage'', funded as project no. CZ.02.01.01/00/22_008/0004617 by Programme Johannes Amos Comenius, call Excellent Research.

References

1 W. Böld and M. Breiter, *Electrochim. Acta*, 1961, **5**, 169–179.
2 H. Jang and J. Lee, *J. Energy Chem.*, 2020, **46**, 152–172.
3 M. van der Merwe, Y. Lee, R. E. Wibowo, T. Kokumai, A. Efimenko, M. D. Arce, C. E. Jimenez, B. Howchen, R. Suarez Anzorena, I. Lucentini, C. Escudero, G. Schuck, Z. Kochovski, M. Favaro, D. E. Starr, K. Reuter, C. Scheurer, M. Bär and R. Garcia-Diez, *Energy Environ. Sci.*, 2025, **18**, 1214–1231.
4 P. Steegstra, M. Busch, I. Panas and E. Ahlberg, *J. Phys. Chem. C*, 2013, **117**, 20975–20981.
5 S. Geiger, O. Kasian, B. R. Shrestha, A. M. Mingers, K. J. J. Mayrhofer and S. Cherevko, *J. Electrochem. Soc.*, 2016, **163**, F3132–F3138.
6 P. Stonehart, H. A. Kozlowska, B. E. Conway and R. G. W. Norrish, *Proc. R. Soc. London, Ser. A*, 1969, **310**, 541–563.
7 F. G. Will and C. A. Knorr, *Z. Elektrochem. Ber. Bunsenges. Phys. Chem.*, 1960, **64**, 270–275.
8 M. W. Breiter, *Z. Phys. Chem.*, 1967, **52**, 73–88.
9 B. Kurnikov, A. Zhurin, V. Cherny, Y. Vasilev and V. Bagotsky, *Elektrokhimiya*, 1973, **9**, 833–836.
10 S. Gottesfeld, *J. Electrochem. Soc.*, 1980, **127**, 1922.
11 L. D. Burke and D. P. Whelan, *J. Electroanal. Chem. Interfacial Electrochem.*, 1981, **124**, 333–337.
12 G. Beni, C. E. Rice and J. L. Shay, *J. Electrochem. Soc.*, 1980, **127**, 1342.
13 V. Birss, R. Myers, H. Angerstein-Kozlowska and B. E. Conway, *J. Electrochem. Soc.*, 1984, **131**, 1502.
14 J. Augustynski, M. Koudelka, J. Sanchez and B. E. Conway, *J. Electroanal. Chem. Interfacial Electrochem.*, 1984, **160**, 233–248.
15 S. H. Glarum and J. H. Marshall, *J. Electrochem. Soc.*, 1980, **127**, 1467.
16 L. D. Burke, J. K. Mulcahy and D. P. Whelan, *J. Electroanal. Chem. Interfacial Electrochem.*, 1984, **163**, 117–128.
17 W. Olthuis, M. A. M. Robben, P. Bergveld, M. Bos and W. E. van der Linden, *Sens. Actuators, B*, 1990, **2**, 247–256.
18 P. G. Pickup and V. I. Birss, *J. Electroanal. Chem. Interfacial Electrochem.*, 1987, **220**, 83–100.
19 L. D. Burke and D. P. Whelan, *J. Electroanal. Chem. Interfacial Electrochem.*, 1984, **162**, 121–141.
20 J. O. Zerbino, N. R. de Tacconi and A. J. Arvía, *J. Electrochem. Soc.*, 1978, **125**, 1266.
21 L. D. Burke and R. A. Scannell, *J. Electroanal. Chem. Interfacial Electrochem.*, 1984, **175**, 119–141.
22 C. Liang, R. R. Rao, K. L. Svane, J. H. L. Hadden, B. Moss, S. B. Scott, M. Sachs, J. Murawski, A. M. Frandsen, D. J. Riley, M. P. Ryan, J. Rossmeisl, J. R. Durrant and I. E. L. Stephens, *Nat. Catal.*, 2024, **7**, 763–775.
23 E. Willinger, C. Massué, R. Schlögl and M. G. Willinger, *J. Am. Chem. Soc.*, 2017, **139**, 12093–12101.
24 B. Lu, C. Wahl, R. dos Reis, J. Edgington, X. K. Lu, R. Li, M. E. Sweers, B. Ruggiero, G. T. K. K. Gunasooriya, V. Dravid and L. C. Seitz, *Nat. Catal.*, 2024, **7**, 868–877.
25 D. B. Rogers, R. D. Shannon, A. W. Sleight and J. L. Gillson, *Inorg. Chem.*, 1969, **8**, 841–849.
26 S. D. James, *J. Electrochem. Soc.*, 1969, **116**, 1681.
27 L. D. Burke and M. McRann, *J. Electroanal. Chem. Interfacial Electrochem.*, 1981, **125**, 387–399.
28 D. A. J. Rand and R. Woods, *J. Electroanal. Chem. Interfacial Electrochem.*, 1974, **55**, 375–381.
29 S. Gottesfeld and S. Srinivasan, *J. Electroanal. Chem. Interfacial Electrochem.*, 1978, **86**, 89–104.
30 B. E. Conway and J. Mozota, *Electrochim. Acta*, 1983, **28**, 9–16.
31 J. Mozota and B. E. Conway, *Electrochim. Acta*, 1983, **28**, 1–8.
32 D. N. Buckley and L. D. Burke, *J. Chem. Soc., Faraday Trans. 1*, 1975, **71**, 1447–1459.
33 E. J. Frazer and R. Woods, *J. Electroanal. Chem. Interfacial Electrochem.*, 1979, **102**, 127–130.
34 D. Michell, D. A. J. Rand and R. Woods, *J. Electroanal. Chem. Interfacial Electrochem.*, 1977, **84**, 117–126.
35 D. N. Buckley, L. D. Burke and J. K. Mulcahy, *J. Chem. Soc., Faraday Trans. 1*, 1976, **72**, 1896–1902.
36 O. Kasian, J.-P. Grote, S. Geiger, S. Cherevko and K. J. J. Mayrhofer, *Angew. Chem., Int. Ed.*, 2018, **57**, 2488–2491.
37 J. Juodkazytė, B. Šebeka, I. Valsiunas and K. Juodkazis, *Electroanalysis*, 2005, **17**, 947–952.
38 C. Luan, M. Corva, U. Hagemann, H. Wang, M. Heidelmann, K. Tschulik and T. Li, *ACS Catal.*, 2023, **13**, 1400–1411.
39 J. M. Otten and W. Visscher, *J. Electroanal. Chem. Interfacial Electrochem.*, 1974, **55**, 1–11.
40 S. Hackwood, A. H. Dayem and G. Beni, *Phys. Rev. B: Condens. Matter Mater. Phys.*, 1982, **26**, 471–478.
41 S. A. Mahmoud, S. M. Al-Shomar and A. A. Akl, *Adv. Condens. Matter Phys.*, 2010, **2010**, 518209.
42 S. Cherevko, S. Geiger, O. Kasian, A. Mingers and K. J. J. Mayrhofer, *J. Electroanal. Chem.*, 2016, **774**, 102–110.
43 S. Cherevko, in *Encyclopedia of Interfacial Chemistry*, ed. K. Wandelt, Elsevier, Oxford, 2018, pp. 68–75, DOI: 10.1016/B978-0-12-409547-2.13569-3.
44 A. BalaKrishnan, N. Blanc, U. Hagemann, P. Gemagami, K. Wonner, K. Tschulik and T. Li, *Angew. Chem., Int. Ed.*, 2021, **60**, 21396–21403.

45 R. Woods, *Isr. J. Chem.*, 1979, **18**, 118–124.
46 L. D. Burke and M. B. C. Roche, *J. Electroanal. Chem. Interfacial Electrochem.*, 1982, **137**, 175–181.
47 L. D. Burke and M. B. C. Roche, *J. Electroanal. Chem. Interfacial Electrochem.*, 1984, **164**, 315–334.
48 L. D. Burke and E. J. M. O'Sullivan, *J. Electroanal. Chem. Interfacial Electrochem.*, 1978, **93**, 11–18.
49 L. D. Burke, M. E. Lyons and D. P. Whelan, *J. Electroanal. Chem. Interfacial Electrochem.*, 1982, **139**, 131–142.
50 S. Hadzi-Jordanov, H. Angerstein-Kozlowska, M. Vukovič and B. E. Conway, *J. Electrochem. Soc.*, 1978, **125**, 1471.
51 L. D. Burke and T. A. M. Twomey, *J. Electroanal. Chem. Interfacial Electrochem.*, 1982, **134**, 353–362.
52 R. D. L. Smith, M. S. Prévot, R. D. Fagan, Z. Zhang, P. A. Sedach, M. K. J. Siu, S. Trudel and C. P. Berlinguette, *Science*, 2013, **340**, 60–63.
53 J. Backholm and G. A. Niklasson, *Sol. Energy Mater. Sol. Cells*, 2008, **92**, 1388–1392.
54 J. Yano, K. Noguchi, S. Yamasaki and S. Yamazaki, *Electrochem. Commun.*, 2004, **6**, 110–114.
55 E. Slavcheva, R. Vitushinsky, W. Mokwa and U. Schnakenberg, *J. Electrochem. Soc.*, 2004, **151**, E226.
56 T. M. Silva, J. E. Rito, A. M. P. Simões, M. G. S. Ferreira, M. da Cunha Belo and K. G. Watkins, *Electrochim. Acta*, 1998, **43**, 203–211.
57 C.-C. Hu and K.-H. Chang, *Electrochim. Acta*, 2000, **45**, 2685–2696.
58 M. Wang, S. Yao and M. Madou, *Sens. Actuators, B*, 2002, **81**, 313–315.
59 K. Pásztor, A. Sekiguchi, N. Shimo, N. Kitamura and H. Masuhara, *Sens. Actuators, B*, 1993, **12**, 225–230.
60 J. Rossmeisl, Z. W. Qu, H. Zhu, G. J. Kroes and J. K. Nørskov, *J. Electroanal. Chem.*, 2007, **607**, 83–89.
61 S. Cherevko, A. R. Zeradjanin, A. A. Topalov, N. Kulyk, I. Katsounaros and K. J. J. Mayrhofer, *ChemCatChem*, 2014, **6**, 2219–2223.
62 C. Minke, M. Suermann, B. Bensmann and R. Hanke-Rauschenbach, *Int. J. Hydrogen Energy*, 2021, **46**, 23581–23590.
63 V. Pfeifer, T. E. Jones, J. J. Velasco Vélez, C. Massué, R. Arrigo, D. Teschner, F. Girgsdies, M. Scherzer, M. T. Greiner, J. Allan, M. Hashagen, G. Weinberg, S. Piccinin, M. Hävecker, A. Knop-Gericke and R. Schlögl, *Surf. Interface Anal.*, 2016, **48**, 261–273.
64 C. Massué, V. Pfeifer, M. van Gastel, J. Noack, G. Algara-Siller, S. Cap and R. Schlögl, *ChemSusChem*, 2017, **10**, 4786–4798.
65 A. Minguzzi, O. Lugaresi, E. Achilli, C. Locatelli, A. Vertova, P. Ghigna and S. Rondinini, *Chem. Sci.*, 2014, **5**, 3591–3597.
66 S. Geiger, O. Kasian, M. Ledendecker, E. Pizzutilo, A. M. Mingers, W. T. Fu, O. Diaz-Morales, Z. Li, T. Oellers, L. Fruchter, A. Ludwig, K. J. J. Mayrhofer, M. T. M. Koper and S. Cherevko, *Nat. Catal.*, 2018, **1**, 508–515.
67 R. V. Mom, L. J. Falling, O. Kasian, G. Algara-Siller, D. Teschner, R. H. Crabtree, A. Knop-Gericke, K. J. J. Mayrhofer, J.-J. Velasco-Vélez and T. E. Jones, *ACS Catal.*, 2022, **12**, 5174–5184.
68 S. Cherevko, *J. Electroanal. Chem.*, 2017, **787**, 11–13.
69 J. Mozota and B. E. Conway, *J. Electrochem. Soc.*, 1981, **128**, 2142.
70 S. Cherevko, S. Geiger, O. Kasian, A. Mingers and K. J. J. Mayrhofer, *J. Electroanal. Chem.*, 2016, **773**, 69–78.
71 M. A. Montero, M. R. G. de Chialvo and A. C. Chialvo, *J. Electroanal. Chem.*, 2016, **783**, 106–111.
72 T. Reier, Z. Pawolek, S. Cherevko, M. Bruns, T. Jones, D. Teschner, S. Selve, A. Bergmann, H. N. Nong, R. Schlögl, K. J. J. Mayrhofer and P. Strasser, *J. Am. Chem. Soc.*, 2015, **137**, 13031–13040.
73 M. Zlatar, D. Escalera-López, M. G. Rodríguez, T. Hrbek, C. Götz, R. Mary Joy, A. Savan, H. P. Tran, H. N. Nong, P. Pobedinskas, V. Briega-Martos, A. Hutzler, T. Böhm, K. Haenen, A. Ludwig, I. Khalakhan, P. Strasser and S. Cherevko, *ACS Catal.*, 2023, **13**, 15375–15392.
74 J. D. E. McIntyre, W. F. Peck and S. Nakahara, *J. Electrochem. Soc.*, 1980, **127**, 1264.
75 J. W. Arblaster, *Platinum Met. Rev.*, 1989, **33**, 14–16.
76 J. L. Ord, *J. Electrochem. Soc.*, 1982, **129**, 335.
77 J. M. Otten and W. Visscher, *J. Electroanal. Chem. Interfacial Electrochem.*, 1974, **55**, 13–21.
78 R. Kötz, H. Neff and S. Stucki, *J. Electrochem. Soc.*, 1984, **131**, 72.
79 S. J. Freakley, J. Ruiz-Esquius and D. J. Morgan, *Surf. Interface Anal.*, 2017, **49**, 794–799.
80 T. Li, O. Kasian, S. Cherevko, S. Zhang, S. Geiger, C. Scheu, P. Felfer, D. Raabe, B. Gault and K. J. J. Mayrhofer, *Nat. Catal.*, 2018, **1**, 300–305.
81 R. M. Kluge, R. W. Haid and A. S. Bandarenka, *J. Catal.*, 2021, **396**, 14–22.
82 J. Xu, L. Chang, Y. Wei, J. Wei, W. Cui, Y. Tao and L. Gan, *ACS Nano*, 2024, **18**, 29140–29151.
83 K. J. J. Mayrhofer, J. C. Meier, S. J. Ashton, G. K. H. Wiberg, F. Kraus, M. Hanzlik and M. Arenz, *Electrochem. Commun.*, 2008, **10**, 1144–1147.
84 L. Tang, B. Han, K. Persson, C. Friesen, T. He, K. Sieradzki and G. Ceder, *J. Am. Chem. Soc.*, 2010, **132**, 596–600.
85 E. F. Holby, W. Sheng, Y. Shao-Horn and D. Morgan, *Energy Environ. Sci.*, 2009, **2**, 865–871.
86 K. J. J. Mayrhofer, B. B. Blizanac, M. Arenz, V. R. Stamenkovic, P. N. Ross and N. M. Markovic, *J. Phys. Chem. B*, 2005, **109**, 14433–14440.
87 J. Mozota, M. Vukovic and B. E. Conway, *J. Electroanal. Chem. Interfacial Electrochem.*, 1980, **114**, 153–157.
88 A. Eftekhari, *Mater. Today Chem.*, 2017, **4**, 117–132.
89 I. T. E. Fonseca, M. I. Lopes and M. T. C. Portela, *J. Electroanal. Chem.*, 1996, **415**, 89–96.
90 V. I. Birss, C. Bock and H. Elzanowska, *Can. J. Chem.*, 1997, **75**, 1687–1693.
91 L. D. Burke and R. A. Scannell, *Platinum Met. Rev.*, 1984, **28**, 56–61.